A numerical model of the Weddell Sea: Large-scale circulation and water mass distribution

Aike Beckmann, Hartmut H. Hellmer, and Ralph Timmermann

Alfred-Wegener-Institute for Polar and Marine Research, Bremerhaven, Germany

Abstract

A circumpolar model for regional studies of the wind-driven and thermohaline circulation of the Southern Ocean including the major sub–ice shelf areas is described. A first series of numerical experiments focusing on the Weddell Sea reveals a pronounced and persistent double-cell structure of the Weddell Gyre with a maximum transport of ~ 60 Sv, in agreement with observations. Experiments with artificial passive tracers point to the shallow shelf areas off the Filchner-Ronne Ice Shelf as main locations for bottom water production. The trajectories of Lagrangian floats are used to determine the pathways and timescales of water mass spreading in the model. In addition, the effect of sub–ice shelf forcing on the water mass characteristics is evaluated. It is shown that water modified in the sub–ice cavities contributes significantly to the deep and bottom water formation along the continental slope, and affects the water mass characteristics throughout the Weddell Sea, by increasing the stability of the near-surface stratification and preventing deep convection.

1. Introduction

The Weddell Sea is one of the few places in the World Ocean where deep and bottom water masses are formed to participate in the global thermohaline circulation. The characteristics of exported water masses are the result of complex interactions between surface forcing, significantly modified by sea ice processes, ocean dynamics at the continental shelf break and slope [*Foldvik et al.*, 1985a; *Muench and Gordon*, 1995] and sub–ice shelf water mass transformations [e.g., *Hellmer and Olbers*, 1989; *Grosfeld et al.*, 1997].

A long-term modeling project, Bremerhaven Regional Ice-Ocean Simulations (BRIOS), has been initiated at the Alfred-Wegener Institute (AWI) to investigate this complex regime, and the role of each component in this system with regard to seasonal, interannual, and decadal variability. A first series of experiments uses a stand-alone ocean model to investigate the large-scale structure of the Weddell Gyre, the relative importance of various water mass formation processes and regions, as well as the pathways of deep and bottom water spreading.

Previous numerical ocean circulation models of the Southern Ocean were mainly interested in the dynamics of the Antarctic Circumpolar Current (ACC) [e.g., *Webb et al.*, 1991] or focussed on the South Atlantic [e.g., *Barnier et al.*, 1998) and did not specifically concentrate on the Weddell Gyre nor on the Antarctic coastal waters. The currently most advanced numerical studies by *Häkkinen* [1995] and *Zhang and Semtner* [1998] use coupled ice-ocean models but exclude the ice shelf cavities. Typically, the model domain extends no farther than 70°S, where an artificial boundary is prescribed. The present study is the first to include the shallow shelf areas as well as the sub–ice shelf cavities of the inner Weddell and Ross Seas in a large-scale ocean circulation model.

This paper describes the design of the model (sections 2 and 3) and a first series of experiments on the characteristics and sensitivities of the Weddell Sea (section 4). A summary is presented in section 5.

2. Model Configuration

2.1. Numerical Ocean Model

The hydrostatic primitive equation ocean circulation model SPEM [*Haidvogel et al.*, 1991] was chosen because its terrain-following vertical coordinate (see Figure 2) is well suited for studies of shelf dynamics and bottom boundary layer flows. With the generalized s coordinate transformation [*Song and Haidvogel*, 1994] given by

$$s = s\left(\frac{z}{H}\right), \qquad (1)$$

where z is depth and $H = H(x, y)$ is the water column thickness, the resulting nonlinear system of equations reads

$$\frac{d(Hu)}{dt} - Hfv = -H\frac{\partial\phi}{\partial x} + \frac{\partial(sH)}{\partial x}\frac{\partial\phi}{\partial s} + \mathcal{F}^u + \mathcal{D}^u \quad (2)$$

$$\frac{d(Hv)}{dt} + Hfu = -H\frac{\partial\phi}{\partial y} + \frac{\partial(sH)}{\partial y}\frac{\partial\phi}{\partial s} + \mathcal{F}^v + \mathcal{D}^v \quad (3)$$

$$\frac{d(H\theta)}{dt} = \mathcal{F}^\theta + \mathcal{D}^\theta \qquad (4)$$

$$\frac{d(HS)}{dt} = \mathcal{F}^S + \mathcal{D}^S \qquad (5)$$

$$0 = -\frac{\partial\phi}{\partial s} - \frac{gH}{\rho_o}\rho \qquad (6)$$

$$0 = \frac{\partial(Hu)}{\partial x} + \frac{\partial(Hv)}{\partial y} + \frac{\partial(H\Omega)}{\partial s} \qquad (7)$$

$$\rho = \rho(S, \theta, z) \qquad (8)$$

where (u, v, Ω) are the (x, y, s) components of the velocity vector $\mathbf{v}$, θ and S are potential temperature and salinity, respectively; ϕ is the dynamic pressure (p/ρ_o), and f and g are the Coriolis parameter and the acceleration of gravity, respectively. The total time derivative is defined as

$$\frac{d(H\alpha)}{dt} \equiv \frac{\partial(H\alpha)}{\partial t} + \frac{\partial(Hu\alpha)}{\partial x} + \frac{\partial(Hv\alpha)}{\partial y} + \frac{\partial(H\Omega\alpha)}{\partial s} \qquad (9)$$

for any prognostic quantity α, and the "vertical velocity" in this s-coordinate system is

$$\Omega(x, y, s, t) = \frac{1}{H}\left(w - u\frac{\partial sH}{\partial x} - v\frac{\partial sH}{\partial y}\right). \qquad (10)$$

Forcing and dissipative terms are denoted as $\mathcal{F}$ and $\mathcal{D}$, respectively.

Equation (8) uses the full nonlinear equation of state (*UNESCO* [1981], modified by *Jackett and Mc-Dougall* [1995] for use with potential rather than *in situ* temperatures) to accurately represent the density structure at the low temperatures on the Antarctic shelves and in the sub–ice shelf cavities.

The model was modified to allow for the inclusion of sub–ice shelf cavities. Our approach is similar to the one described by *Grosfeld et al.* [1997]: the upper boundary of the ocean model conforms to the ice shelf base. However, unlike in the work by *Grosfeld et al.* [1997], no coordinate lines run into the ice shelf. Our strategy leads to a few relatively simple modifications of the ocean model. The upper boundary is no longer at $z = 0$ but follows the ice shelf base at $z = -h$ (see Figure 2). The hydrostatic pressure at

the base is required to compute the horizontal pressure gradient in the ocean model. Assuming that the ice shelf is in isostatic equilibrium, this pressure can be approximated by the integral over depth of the reference density profile:

$$\phi(-h) = -\frac{g}{\rho_o} \int_o^{-h} \rho_w \, dz \qquad (11)$$

where $\phi(-h)$ is the pressure at the ocean's upper boundary and $\rho_w = 1028.4$ kg m^{-3} is the average *in situ* density of the water replaced by the ice.

2.2. Model Domain and Grid
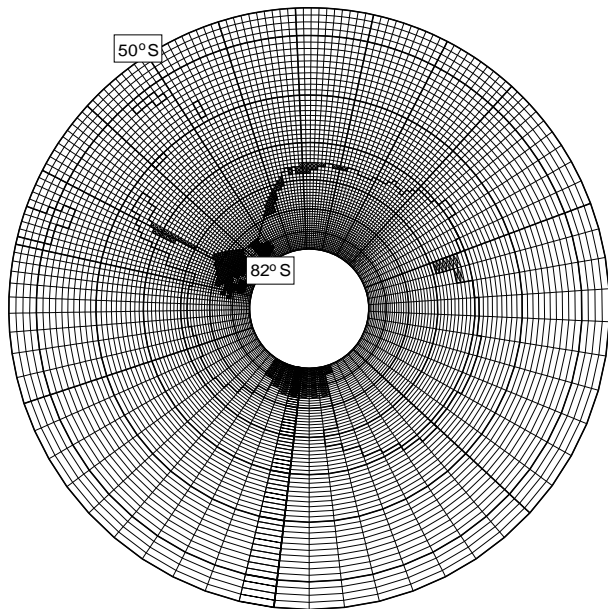
Figure 1. Bremerhaven Regional Ice-Ocean Simulations (BRIOS 1) circumpolar model grid. Ice shelf areas are marked by shaded grid boxes.

The basic configuration for studies in the framework of BRIOS is a periodic circumpolar domain between 82°S and 50°S. By covering the whole Southern Ocean, circumpolar influences on the Weddell Gyre can be considered.

BRIOS 1 is our coarse resolution, stand-alone ocean model. The horizontal grid focuses on the Weddell Sea sector, where the resolution is isotropic (1.5° in the zonal, 1.5°cosΦ in the meridional direction; see Figure 1). This results in a grid spacing of $\sim$ 100 km at the northern boundary and 20 km at the southern edge. Outside the Weddell sector, zonal grid spacing increases gradually to 6.75°. Although coarser than necessary for eddy-permitting studies, which would require grid spacing of the order of the first internal

Rossby radius of deformation (5-10 km), the resolution allows for principal studies of water mass formation and spreading and a large number of sensitivity runs.
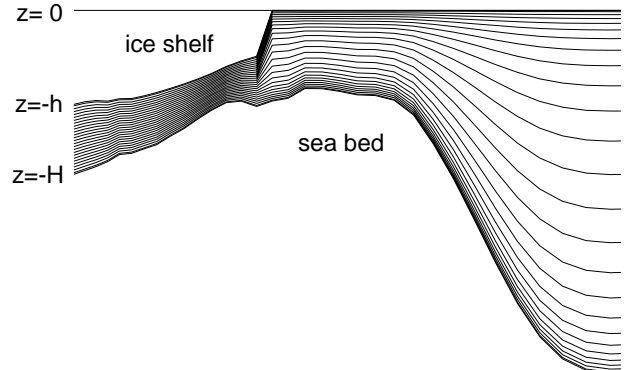
Figure 2. Vertical discretization in the presence of an ice shelf: The levels are stretched nonlinearly toward surface and bottom. The minimum water column thickness is 200 m.

In the vertical, 24 levels, nonequidistantly distributed in the water column, are used. Higher resolution near the surface and bottom (with grid spacings between 10 and 30 m) permits reasonable representation of the upper and lower boundary layers (Figure 2).

2.3. Topography, Islands, and Ice Shelves

The bottom topography (Figure 3a) was taken from the satellite gravimetry derived 2′ resolution data set of *Smith and Sandwell* [1997]. For the Weddell Sea, south of 72°S, this is supplemented by recent data from the AWI bathymetry group [*Schenke et al.*, 1998] and the *Johnson and Smith* [1997] Filchner-Ronne sub–ice cavity data set. The data were interpolated bilinearly to the model grid points. A moderate smoothing of the topography was performed: the minimum water column thickness was set to 200 m, and the r value [*Beckmann and Haidvogel*, 1993]

$$r = \frac{h_{+1/2} - h_{-1/2}}{h_{+1/2} + h_{-1/2}} \qquad (12)$$

was limited to 0.2 (except for the ice shelf edge, where maximum values of 0.3 were permitted). This parameter is a rough measure of the pressure gradient error in terrain-following coordinate models, which can drive an along-topography flow in the direction of topographic waves, depending on the local density profile. For the weak stratification in the Southern Ocean this error presents no serious problem.

Five islands (Figure 3a) are explicitly included in the simulation: the South Georgia, South Orkney,

and South Sandwich Island complexes, and two sub–ice shelf islands (Berkner Island and the combined Henry and Korff Ice Rise structure). Owing to the relatively coarse resolution, other islands are only represented by their topographic signature with a minimum depth of 200 m.
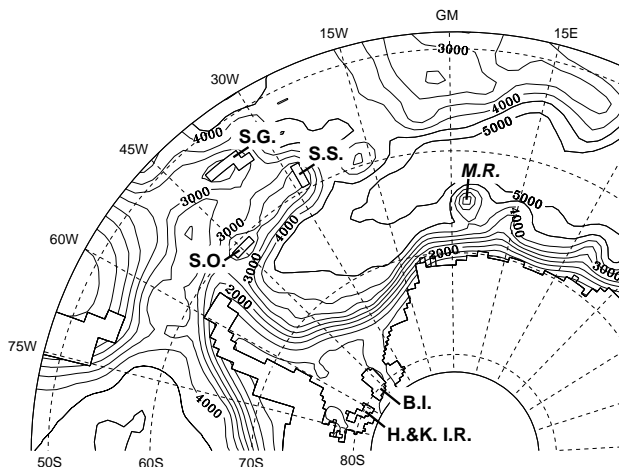
Figure 3a. Topography and islands of the Weddell Sea sector as represented by BRIOS 1. Included are the South Georgia (S.G.), South Sandwich (S.S.), and South Orkney (S.O.) islands, as well as Berkner Island (B.I.) and the Henry and Korff Ice Rises (H. and K.I.R.). The location of Maud Rise (M.R.) is also highlighted. GM denotes the Greenwich meridian.
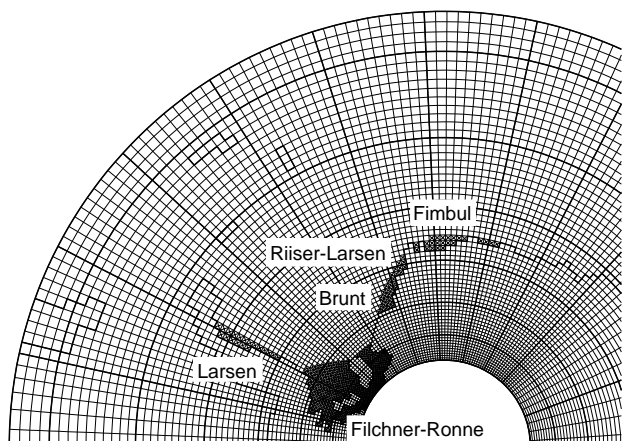
Figure 3b. Grid and ice shelves for the Weddell Sea sector of BRIOS 1.

The two major Antarctic ice shelves, Filchner-Ronne and Ross, are included with as much detail as possible [*Johnson and Smith*, 1997]. Ice thickness was filtered to remove grid-scale variability. All other ice shelves (Larsen, Brunt, Riiser-Larsen, Fimbul, and Amery) are included in a cruder way, owing to the lack of detailed bathymetric and ice thickness data, coarse grid resolution in the relevant sector, or relatively minor importance. Their thickness is assumed

to be constant at 200 m. In our analysis, Fimbul, Riiser-Larsen, and Brunt (see Figure 3b) are treated as one complex called the Eastern Weddell Ice Shelf (EWIS).

2.4. Subgrid-Scale Parameterizations

Harmonic viscosity and diffusivity operators $\mathcal{D}$ are used with spatially varying coefficients. This was found helpful for grids of strongly varying resolution. The lateral viscosity was chosen to be a quadratic function of the horizontal grid spacing Δ,

$$\nu_{u,v} = 5 \times 10^{-6} \text{ s}^{-1} \, \Delta^2 \quad . \tag{13}$$

A linear boundary layer stress is applied both at the seafloor and the base of the ice shelves.

The lateral diffusivity depends linearly on grid spacing and local flow field and resembles an upstream scheme acting along geopotential surfaces to avoid the large implicit vertical diffusivity of along-coordinate mixing operators [see *Beckmann and Haidvogel*, 1997; *Barnier et al.*, 1998]. At the surface and the bottom, an additional grid-spacing-dependent background diffusivity of

$$\nu_{T,S} = 2 \times 10^{-2} \text{ m s}^{-1} \Delta \tag{14}$$

was added to represent the wind-induced, near-surface mixing and the enhanced levels of turbulence in the bottom boundary layer.

Vertical viscosity and diffusivity are computed as Richardson-number-dependent functions, according to *Pacanowski and Philander* [1986]. This includes a maximum diffusivity of $\kappa = 0.01$ m^2 s^{-1} in case of small and negative Richardson numbers. An explicit scheme has been employed for vertical diffusivity.

A large number of initial parameter studies have been performed to determine the sensitivity to the subgrid scale parameterization. In summary, the vertical diffusivity was found to be the most critical term. The weak stratification in this salinity-dominated regime reacts very sensitively to large vertical diffusivities, such that instantaneous convective adjustment leads to rapid homogenization of the central Weddell Sea down to 2000 m. In contrast, the maximum vertical diffusivity of 0.01 m^2 s^{-1} means that, given continuous forcing, convective processes can homogenize a 30 m thick water column in ~ 1 day, a reasonable assumption for grid cells that cover hundreds to thousands of square kilometers, averaging over many individual convective plumes and the corresponding upwelling areas.

2.5. Time Stepping

The model time step is mainly limited by vertical advection over the shallow shelf areas; it is set to 11.25 min (128 time steps per day). The year is assumed to consist of 12 months with 30 days each.

3. Model Initialization and Forcing

3.1. Model Initialization and Lateral Boundary Conditions

The initial fields stem from the Hydrographic Atlas of the Southern Ocean (HASO) [*Olbers et al.*, 1992], trilinearly interpolated to the model grid. Since no gridded hydrographic data are available for the sub–ice shelf areas, linear potential temperature and salinity profiles were prescribed. As the hydrographic data are more representative of austral summer conditions, the model integration begins in January. Starting from a state of rest, the model is integrated diagnostically for 1 year (i.e., with strong restoring of the temperature and salinity fields to the HASO data). During this period, no external forcing is applied and the hydrography within the ice shelf cavities can adjust to the forcing at the upper boundary and the outside HASO values. After that, model time is reset to zero, the interior restoring is removed, and the full surface forcing is applied.

The northward limitation of the model domain to 50°S requires a partial prescription of the ACC. Its transport was set to 130 Sv (1 Sv = 10^6 m^3 s^{-1}) in the Drake Passage. Half of this transport leaves the domain between the tip of South America and 30°W. These 65 Sv are gradually fed back into the model domain in the Indian Ocean sector between 120°E and 180°E. In a buffer zone of five grid points at the northern boundary, temperatures and salinities are strongly restored to HASO climatological fields.

3.2. Surface Forcing
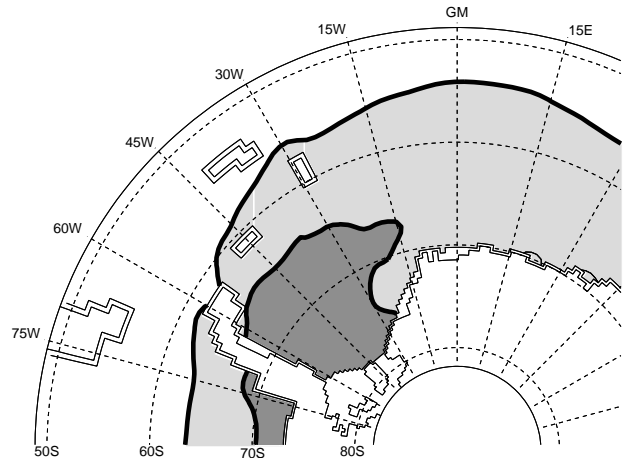
Figure 4. Climatological monthly mean sea ice coverage (as defined by the 15% ice concentration isoline) in BRIOS 0 for March (dark shading) and September (light shading), the months of minimum and maximum ice extent, respectively.

The ocean model is forced by a seasonal cycle of sea surface temperature, freshwater flux, and surface stress. These forcing fields are taken from a stand-alone sea ice/mixed layer model (called BRIOS 0) on the same horizontal grid as BRIOS 1. Its dynamic-thermodynamic formulation is based on *Hibler* [1979] and *Lemke et al.* [1990]. Indicative of the seasonal cycle of the surface forcing data is the mean minimum and maximum sea ice extent from the sea ice model (Figure 4).

The mixed layer temperature in both ice-covered and ice-free regions of the model domain is derived from a surface energy budget computed by the mixed layer model. This includes the surface fluxes of sensible and latent heat as well as the surface radiation budget and the vertical entrainment heat flux from the ocean below the pycnocline. The turbulent heat flux between ocean and sea ice is computed as

$$Q_{oi} = \rho_w c_{pw} \frac{H_{ML}}{\Delta t} \left(T_{ML} - T_f \right) \quad , \qquad (15)$$

where ρ_w is the constant density of seawater, c_{pw} is the heat capacity of water at constant pressure, and H_{ML} and T_{ML} are the depth and temperature of the mixed layer, respectively. T_f is the constant freezing temperature (-1.86°C), and Δt is the time step (6 hours) for BRIOS 0. Using this formulation, we assume that the coupled system of sea ice and oceanic mixed layer aspires to an equilibrium in which the mixed layer temperature is at the freezing point. Deep ocean boundary conditions are again taken from HASO.
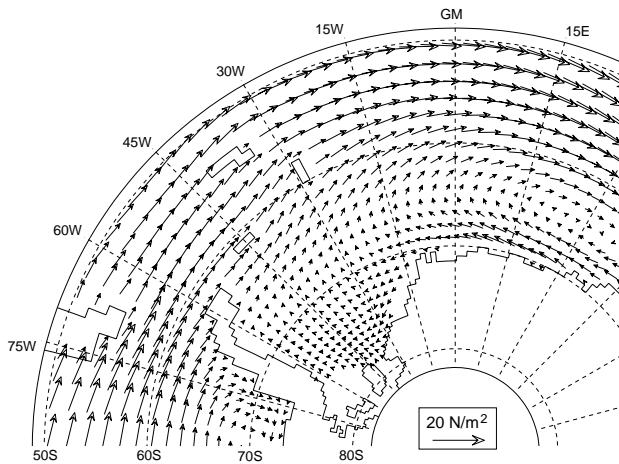
Figure 5a. Annual-mean sea surface stress [N m^{-2}] at the ocean surface, obtained from the stand-alone sea ice model BRIOS 0.
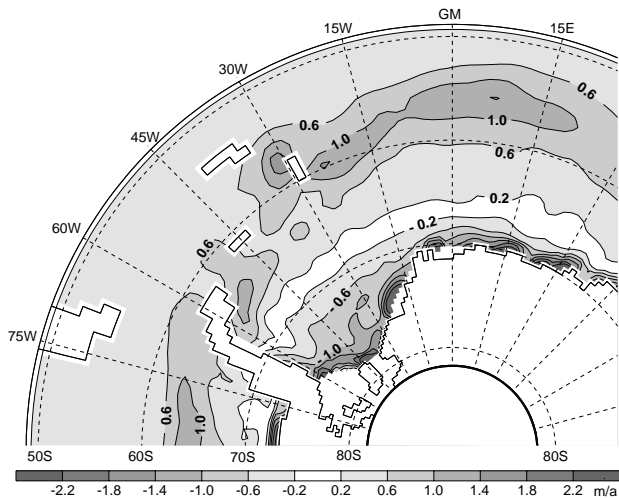
Figure 5b. Annual-mean net fresh water flux [m yr^{-1}] into the ocean surface obtained from the stand-alone sea ice model BRIOS 0. Contour interval is 0.4 m yr^{-1}. Areas of maximum input of either fresh water or salt are shaded in the darkest grey.

For the ocean model runs, the thermal forcing is implemented through a restoring of the sea surface temperature (SST) to the linearly interpolated monthly mean mixed layer temperatures of the sea ice model. The restoring timescale is chosen to be linearly proportional to the thickness Δz_s of the uppermost model grid box (which varies between 10 and 30 m owing to the coordinate transformation):

$$\lambda^{-1} = 86,400 \text{ m}^{-1} \text{ s}^{-1} \Delta z_s \quad . \tag{16}$$

In contrast, the salt flux $\mathcal{F}^S$ is converted directly from the sea ice model's freshwater flux $\mathcal{F}^W$ (reference salinities are taken from the HASO). In ice-covered areas, the freshwater flux is derived from the freezing and melting rates of sea ice and/or snow. In open water areas, the freshwater flux is given by a precipitation rate of 35 cm yr^{-1} [*Parkinson and Washington,* 1979], chosen to be constant in time and space over the whole model domain. In addition, a weak restoring (with a 300-day relaxation timescale) to HASO salinities is applied.

Like the fluxes of heat and salt, the surface momentum fluxes are averaged over the ice-covered and the open water parts of each grid cell, weighted by the ice concentration. In the ice-free part, the ocean surface stress is derived from 10-m winds $\mathbf{v}_{10}$ using the standard bulk formula

$$\boldsymbol{\tau}_a = \rho_a c_a \left| \mathbf{v}_{10} \right| \mathbf{v}_{10} \quad , \tag{17}$$

where ρ_a is air density and $c_a = 1.32 \times 10^{-3}$ is the drag coefficient. The stress at the ice-ocean interface is part of the momentum balance in the sea ice model and computed as

$$\boldsymbol{\tau}_w = \rho_w c_w \left| \mathbf{v}_w - \mathbf{v}_{ice} \right| \left(\mathbf{v}_w - \mathbf{v}_{ice} \right) . \tag{18}$$

In analogy to (17), $c_w = 3 \times 10^{-3}$ is the drag coefficient between ice and ocean; $\mathbf{v}_w$ and $\mathbf{v}_{ice}$ are the (horizontal) velocities of ocean and sea ice, respectively. Using this equation, we assume that no rotation angle exists between the velocities of the uppermost layer of the ocean model and the surface velocities.

The sea ice model is driven with 6-hourly data of 10-m wind, total cloudiness, 2-m air, and dew point temperatures of the European Center for Medium-Range Weather Forecasts (ECMWF) reanalyses of 1985-1993. Two passes of this 9-year period were used to obtain a quasi-stationary seasonal cycle of the sea ice distribution. From the third 9 years of integration, fluxes of momentum and fresh water at the ocean surface (Figure 5a and 5b) as well as the mixed layer temperature are averaged to climatological monthly mean values. These are employed as surface forcing for all experiments with the ocean model.

3.3. Sub-Ice Shelf Forcing

The heat and salt balances at the ocean-ice shelf boundary can be described as [see, e.g., *Hellmer et al.,* 1998]

$$\rho_i (L - c_{pi} \Delta T) \dot{h} = \rho c_{pw} \gamma_T (T_b - T_w) \quad , \tag{19}$$
$$\rho_i S_b \dot{h} = \rho \gamma_S (S_b - S_w) \quad , \tag{20}$$

where for the total heat flux across the interface both the amount of heat consumed by melting ($\dot{h} < 0$) or

released by freezing ($\dot{h} > 0$), and the vertical molecular diffusive heat flux through the ice shelf is considered. Here the freezing rate $\dot{h}$ is defined as negative for melting, $\rho_i = 920$ kg m^{-3} is the average ice density, $c_{pi} = 2000$ J (kg $^\circ$C)$^{-1}$ the specific heat capacity of ice, $L = 3.34 \times 10^5$ J kg^{-1} is the latent heat of fusion, and ΔT is the temperature difference between the ice shelf interior and the *in situ* freezing temperature at its base. The dilution caused by melting or the salt input as a result of freezing is proportional to the salinity S_b at the ice shelf base.

The oceanic fluxes of salt and heat at the ocean/ice shelf boundary are parameterized by diffusive fluxes proportional to the respective difference between the temperature T_b and salinity S_b at the ice shelf base and the ocean *in situ* temperature T_w and salinity S_w which are taken from the uppermost grid point in each sub–ice shelf water column. Here $c_{pw} = 4000$ J (kg $^\circ$C)$^{-1}$ is the heat capacity of seawater at 0°C. The turbulent exchange coefficients for heat and salt are chosen constant ($\gamma_T = 10^{-4}$ m s^{-1}; $\gamma_S = 5.05 \times 10^{-7}$ m s^{-1} [*Hellmer and Olbers*, 1989].

To close this nonlinear system, a linearized version of the equation for the freezing point of seawater [*Foldvik and Kvinge*, 1974] is used:

$$T_b = 0.0939^\circ\text{C} - 0.057^\circ\text{C} S_b + 7.64 10^{-4\circ}\text{C m}^{-1} h \quad (21)$$

which leads to a system of three nonlinearly coupled equations. Elimination of $\dot{h}$ yields a quadratic equation for salinity S_b, which can be solved by discarding unphysical negative salinities. The resulting heat and salt fluxes are used to force (4) and (5) through the application of flux boundary conditions at the surface.

4. Model Results

This section presents the main characteristics of the modeled circulation and water mass distribution in the Weddell Sea sector of the Southern Ocean. We look at Weddell Gyre strength and structure, the Antarctic Coastal Current, and water mass formation sites. An assessment of the results is performed by comparison with observations.

4.1. Annual Mean Circulation

After 15 years of adjustment, a quasi-stationary circulation pattern has evolved. The remaining interannual trends in domain-averaged temperature and salinity are small ($-5 \times 10^{-4\circ}$C yr^{-1} and 2×10^{-4} psu yr^{-1}, respectively).
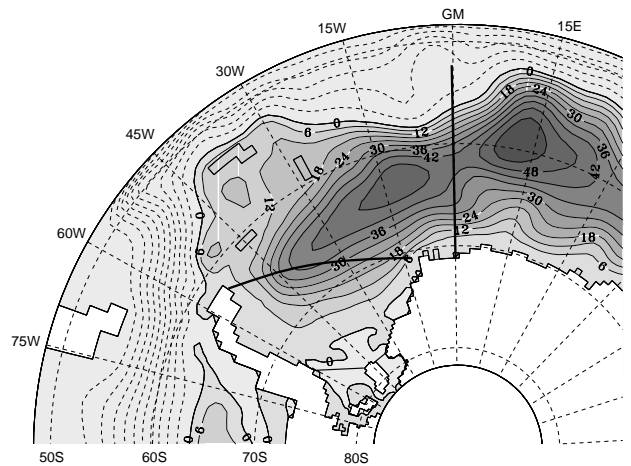

Figure 6. Annual-mean transport stream function for year 20 in the Weddell Sea sector of the Southern Ocean, showing a pronounced double-cell structure of the Weddell Gyre. Intervals are 6 Sv for positive and 12 Sv for negative contours. Lines mark the approximate locations of repeated hydrographic and current meter sections [*Fahrbach et al.*, 1994; *Schröder and Fahrbach*, 1999].

The annual-mean, vertically integrated transport is shown in Figure 6. The most striking feature of the stream function field is the double-cell structure of the Weddell Gyre. As suggested by the hydrographic observations of *Mosby* [1934] and *Bagriantsev et al.* [1989], our numerical experiments show one cell filling the western Weddell Basin and another (in our simulations even stronger) one trapped in a deeper basin northeast of Maud Rise. Both maxima exceed 50 Sv in the annual mean and proved to be a very robust feature throughout our parameter sensitivity studies. Quantitatively, the simulated transport compares well with calculations by *Fahrbach et al.* [1994] along the Joinville Island-Kapp Norvegia section (30 ± 10 Sv) as well as more recent measurements by *Schröder and Fahrbach* [1999] along the Greenwich meridian (60 ± 10 Sv). The double-cell structure persists throughout the year but is most pronounced in austral winter.

Information on the three-dimensional flow field can be extracted from drifter trajectories, evenly seeded across the model domain at a constant depth and integrated in time for 5 years. The double-cell structure of the Weddell Gyre is less evident from the surface drifter tracks (Figure 7a), which reveal an intensified coastal current band. The northeastward surface flow is branching around the South Sandwich Islands and splits into three almost zonal frontal bands. Farther east, there is divergent flow along the 63°S latitude circle (Figure 7a, dotted line). At 50-m depth the direct influence of the wind is dominant. The model results are consistent with buoy data, showing no recirculation northeast of Maud Rise [*Kottmeier and*

Sellmann, 1996].
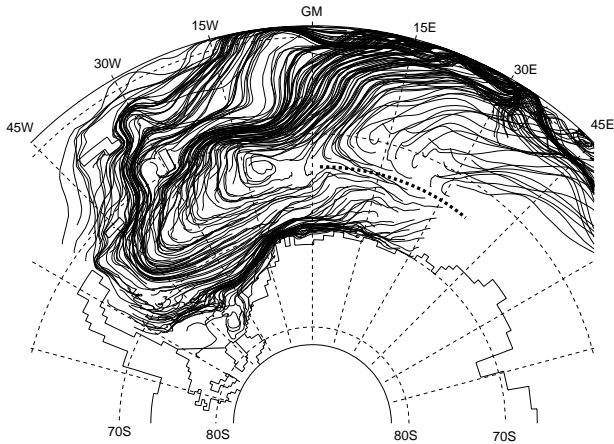
Figure 7a. Five-year trajectories of near-surface (∼50 m) drifters released in year 15 of the integration. The dotted line marks the surface flow divergence in the eastern Weddell Sea.
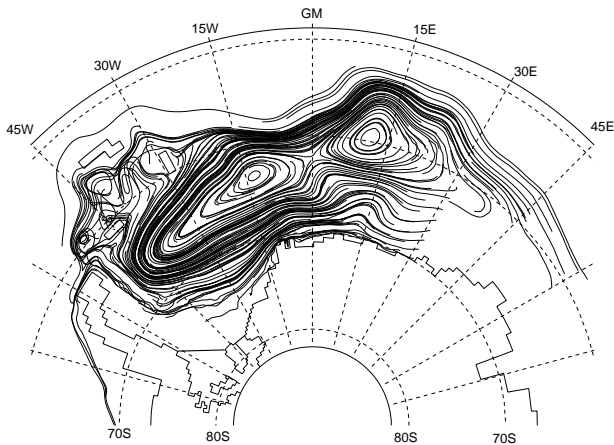

Figure 7b. Five-year trajectories of subsurface (∼1000 m) drifters released in year 15 of the integration.

In contrast, the subsurface floats (Figure 7b) clearly mark the double-cell structure. Typical time-mean velocities at this depth are up to 1.5 cm s^{-1}. Particles circulate smoothly with only little seasonal and/or interannual fluctuations. The Scotia Sea, however, is characterized by higher variability. Note also that some floats escape westward from the Weddell into the Bellingshausen Sea.

The length of the float trajectories is indicative of the advective timescale in different areas. While the residence time in the middepth central Weddell Sea is typically several decades, it is only a few years within the coastal current and at the northern rim current.

The modeled westward flowing southern limb of the Weddell Gyre is largely barotropic (i.e., vertically

unsheared), with 15 cm s^{-1} maximum instantaneous flow and ∼ 5-6 cm s^{-1} time-mean velocities (Figure 8a). This agrees well with *Fahrbach et al.*'s [1994] measurements. There is a general onshore component in the surface layers and a systematic downslope flow near the bottom. Even the surface circulation reflects the presence of topographic features like Maud Rise and other promontories along the Antarctic coast. At this resolution, coastal current instabilities cannot be expected to evolve. However, the narrowness of the front is well represented and leads us to conclude that noneddy-resolving models can represent the Weddell Gyre circulation quite realistically.
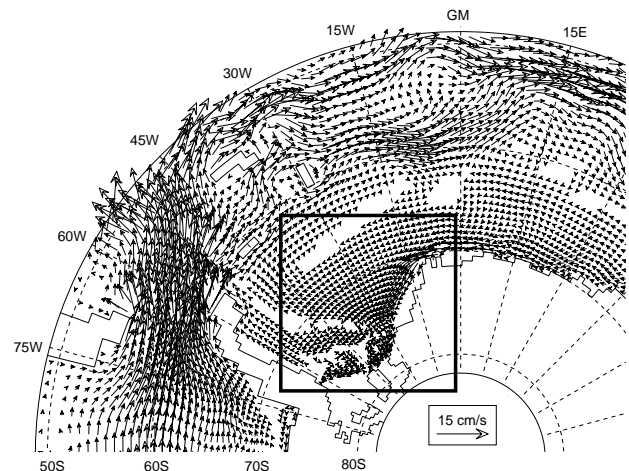
Figure 8a. Annual mean of the near-surface flow. White areas represent velocities smaller than 3 cm s^{-1}. The rectangular marks the area shown in Figure 8b.
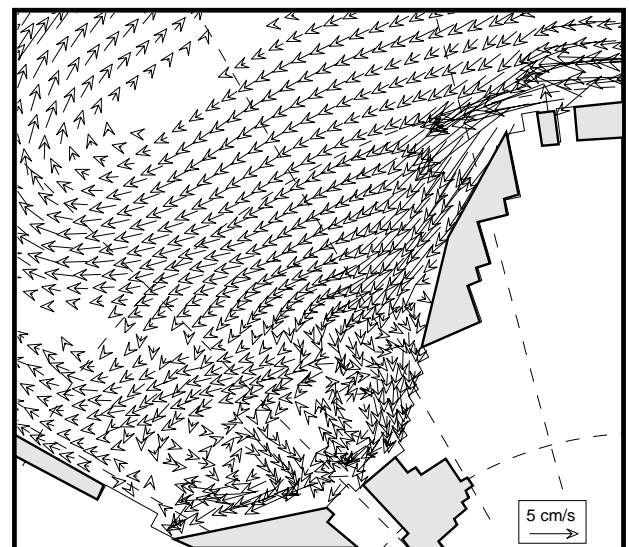

Figure 8b. Enlargement of the interior Weddell Sea, showing the Antarctic Coastal Current separation area off Brunt Ice Shelf. White areas represent velocities smaller than 2 cm s^{-1}. Shaded areas mark the ice shelves.

A closer look at the southern part of the Weddell Sea shows that the coastal current splits off Brunt Ice Shelf (Figure 8b); the stronger offshore branch follows the 2000- to 2500-m depth contour, while a second, onshore branch continues in 500- to 1000-m deep water. Farther south, the model shows a cyclonic surface circulation in the Filchner Trough, as observed by *Carmack and Foster* [1975]. A weak cyclonic cell (of ∼ 0.6 Sv) can also be detected in the annual-mean, vertically integrated transport. However, the sense of the Filchner Trough circulation changes with season, with a period of anticyclonic flow in winter, caused by salt input from freezing along the southeastern Weddell Sea coast and shelf ice edge.

4.2. Hydrographic Structure
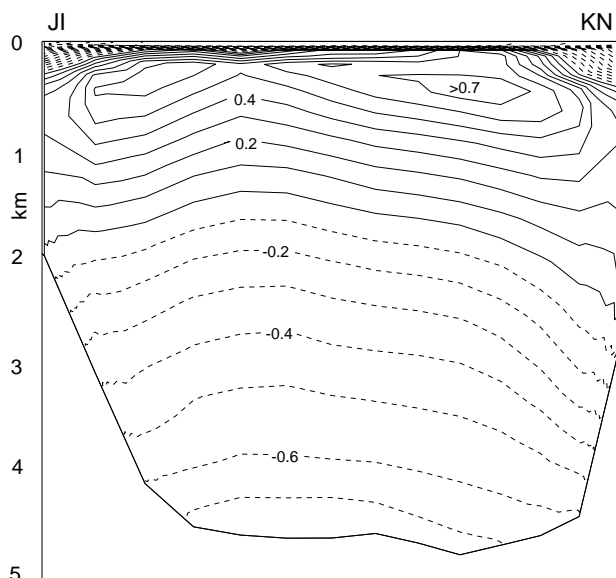
Figure 9a. Simulated annual mean potential temperature on *Fahrbach et al.*'s [1994] transect from Joinville Island (JI) to Kapp Norvegia (KN) (the near-zonal line in Figure 6.
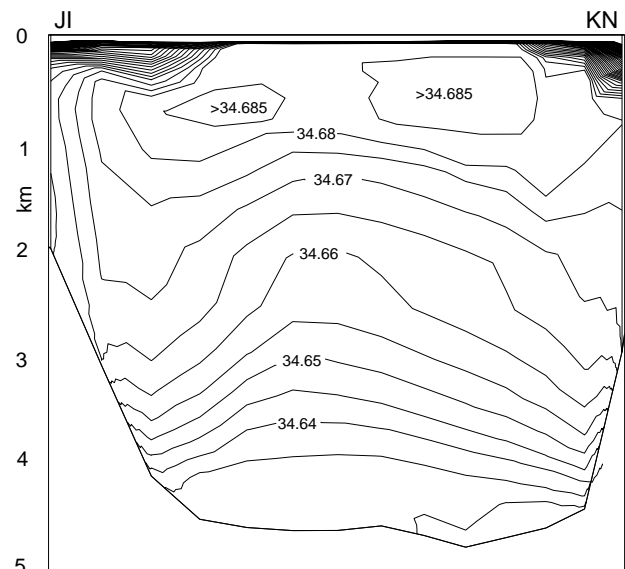
Figure 9b. Same as Figure 9a, but for salinity.

Validation of the model results against observations are based on the sections by *Fahrbach et al.* [1994], who have compiled repeated hydrographic measurements along a transect between Joinville Island near the Antarctic Peninsula and Kapp Norvegia on the EWIS coast. Figures 9a and 9b show the modeled annual mean hydrographic conditions along that section. Modeled potential temperatures show a subsurface maximum of 0.75°C in ∼ 400 m and a doming in the central Weddell Sea. Bottom temperatures are slightly too warm; this might be due to insufficient bottom boundary layer transport of cold water from the continental shelves off the Antarctic Peninsula. The salinity field also indicates the doming in the central Weddell Sea and a downslope transport on the northwestern side of the transect: relatively fresh waters with salinities < 34.68 psu reach down to 3000 m. Consequently, the deep structure of the salinity field is in good agreement with the observations. However, the subsurface salinity maximum is too large in both horizontal and vertical extent.

4.3. Seasonal Cycle
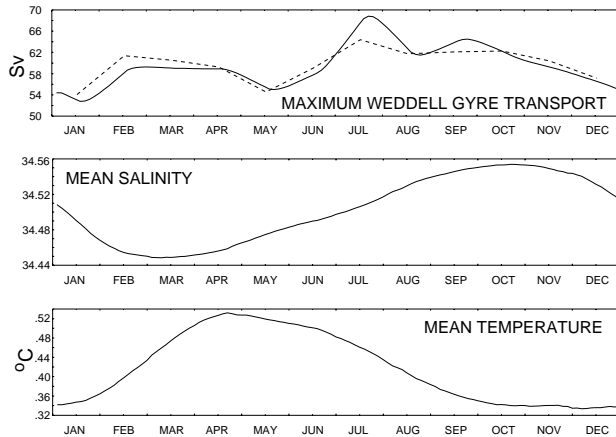
Figure 10. Time series of the (top) maximum Weddell Gyre transport (solid line), and the curl of the wind stress (dashed line), (middle) salinity and (bottom) temperature averaged over the top 250 m in the Weddell Sea sector of BRIOS 1.

The temporal behavior of the Weddell Gyre circulation in the model is demonstrated by time series of the maximum Weddell Gyre transport and the volume-averaged temperature and salinity for the Weddell Sea sector (Figure 10). The transport varies between 52 and 69 Sv, with the minimum in January and the maximum in July. This variation corresponds closely with the area-averaged wind stress curl. Most of the seasonal transport variability can be explained as the direct effect of the wind forcing. An exception is the increased transport in July, during the period of maximum sea ice formation.

The seasonal signals of temperature and salinity show the natural phase lag, in that the minimum salinity leads the temperature maximum by 2 months. This is due to the consumption of heat for melting sea ice prior to the warming of the surface waters. These processes are properly included in the surface fluxes from the stand-alone sea ice model BRIOS 0.

4.4. Deep Water Formation Regions

Since the Weddell Sea is one of the main water mass formation regions of the World Ocean, special attention is given to formation sites and pathways of Weddell Sea's deep water. At its current resolution, the model cannot reproduce fast decending plumes of dense water, one of the important mechanisms for downslope spreading of dense water [see *Baines and Condie*, 1998]. However, the terrain-following vertical coordinate used here allows for a slow advective/diffusive spreading of bottom waters into the abyss, and their net effect on the large scale is found

to be quite representative of the small-scale processes occurring in the ocean.
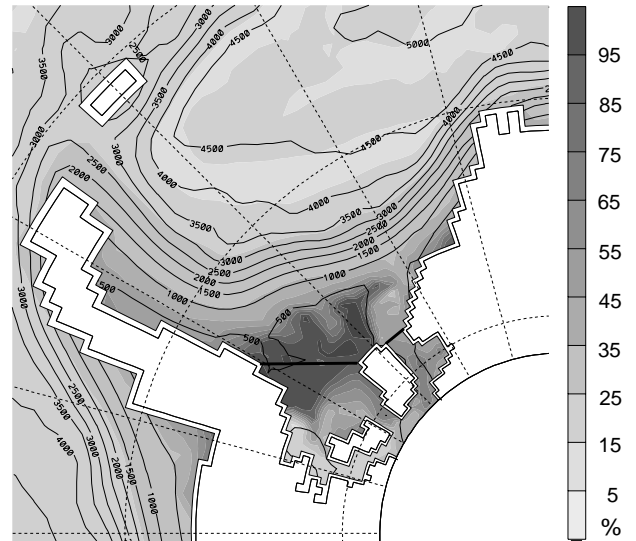
Figure 11. Concentration of a passive tracer in the bottom layer, 5 years after initial uniform release at the surface, on top of selected bottom depth contours.

To identify the spreading of newly formed dense water, an artificial passive tracer has been released continuously and uniformly distributed at the surface of the Weddell Sea. The resulting distribution of this tracer in the bottom layer, 5 years after its initial release at the surface, is shown in Figure 11. The highest concentrations are found on the Berkner and General Belgrano Banks as a result of deep convection during austral winter. There are at least two separate pathways for these water masses: northward down the continental slope and southward, mainly into the Ronne sub–ice cavity. The former reaches the tip of the Antarctic Peninsula within a few years, in agreement with a 2-year estimate based on tracer observations [*Mensch et al.*, 1996]. The latter recirculates in the sub–ice cavity, thus becoming the source water for Ice Shelf Water (ISW), characterized by temperatures below the surface freezing point [*Carmack and Foster*, 1975]. Such sub–ice circulation compares well with the circulation scheme proposed by *Nicholls and Makinson* [1998] for the western Ronne cavity.
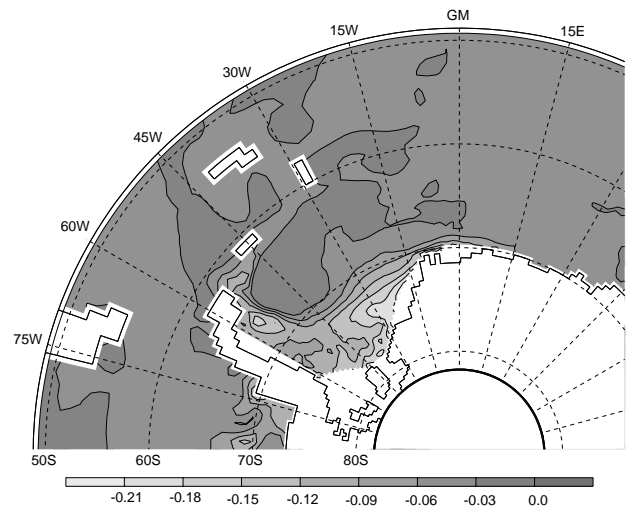
4.5. Effect of Sub-Ice Shelf Forcing

One of the novel aspects of this study is the inclusion of sub–ice shelf areas and the ocean-ice shelf interaction in a large-scale ocean circulation model. In this section we will evaluate the impact of these processes on the hydrography of the Weddell Sea.
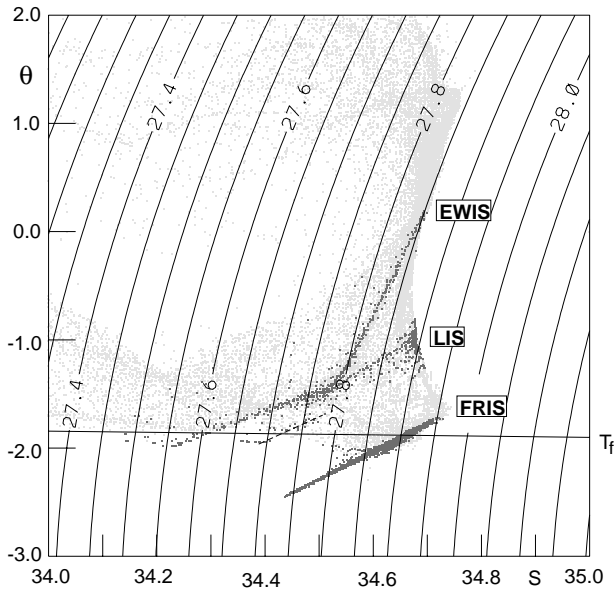
Figure 12. Annual-mean θ-S diagram in the Weddell sector. Darker dots indicate water masses within the cavities. FRIS is the Filchner-Ronne Ice Shelf, LIS the Larsen Ice Shelf. The dashed line indicates the Eastern Weddell Ice Shelves (EWIS) melting line.

The sub–ice shelf areas are sources of relatively cold and fresh water masses, as evident from the modeled θ-S diagram for the Weddell Sea sector (Figure 12). Each cavity has its own signature determined by melting of meteoric ice into seawater [*Gade*, 1979]. With similar slopes of $\sim$2.5°C psu^{-1} the locations of the melting curves differ in θ-S space owing to the different characteristics of the source water masses [*Nøst and Foldvik*, 1994]. The additional, steeper EWIS slope indicates the characteristics of deep water as it flows parallel to the coast beneath parts of the ice shelf, which floats over the deeper ocean. The modification occurs owing to mixing with meltwaters resulting from local ocean/ice shelf interaction (dashed line between Larsen Ice Shelf (LIS) and Filchner-Ronne Ice Shelf (FRIS) in Figure 12). As evident from observations [*Foldvik et al.*, 1985b; *Nicholls*, 1996], the coldest water mass (-2.5°C) is produced in the FRIS cavity. LIS and EWIS also produce water masses slightly cooler than the surface freezing point. However, with lower density than the FRIS-ISW, these meltwaters might influence the upper ocean rather than the Weddell Sea abyss.

Figure 13a. Annual-mean salinity difference without sub–ice shelf forcing in 100-m depth for year 20 of the simulation.
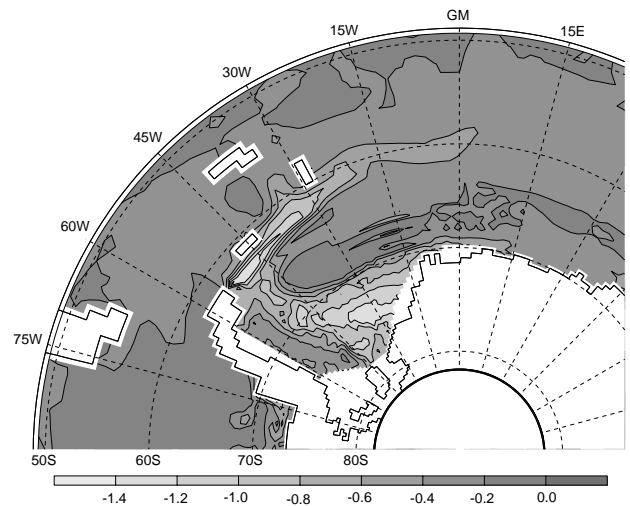
Figure 13b. Same as Figure 13a, but for potential temperature.

High-salinity shelf water ($>$34.75) at the surface freezing point is not evident in the modeled θ-S diagram (Figure 12) owing to the representation of an annual mean. However, for deep waters the θ-S curve shows the linear mixing between Warm Deep Water and Weddell Sea Deep Water. A benthic layer consisting of a low-salinity and a high-salinity bottom water type, in agreement with observations from the western Weddell [*Gordon et al.*, 1993; *Fahrbach et al.*, 1995], represents the densest water of the deep Weddell Sea. Since characteristics of this benthic layer are also found beneath LIS, we assume that near-bottom waters from the Larsen Shelf sink down the continental slope without vigorous mixing to contribute to the low-salinity bottom water type [*Gordon et al.*, 1993].

In addition, those shelf waters penetrating into the LIS cavity produce a low-salinity, low-density ISW which might contribute as surface water to the formation of new bottom water owing to mixing at the slope front [*Gordon*, 1998]. The injection of glacial meltwater into the benthic layer off Larsen Ice Shelf was suggested by the tracer studies of *Weppernig et al.* [1996].

To further investigate the effects of the sub–ice shelf forcing, a sensitivity run was performed, disabling the ocean-ice shelf interaction. The resulting annual-mean salinity and temperature distribution after 20 years shows significant differences in the near-surface water properties (see Figures 13a and 13b). With sub–ice shelf forcing, the near-surface layers are distinctively fresher (up to -0.22 psu) and cooler (up to -1.5°C), as the ice shelves represent a continuous source of lighter water masses. The injection into the Weddell Gyre mainly occurs near EWIS, where the cavity flushing rate is high. As a result, there is a wake of fresher water originating from ice-shelf-ocean interaction, which can be traced downstream to the tip of the Antarctic Peninsula. While the temperature difference (Figure 13b) is more pronounced and can be felt even at the northern rim of the Weddell Gyre, the salinity difference is dynamically more important owing to the density dependency on salinity in this cold environment. The presence of this lighter water stabilizes the stratification of the water column, reduces convection, and preserves the warmer and saltier deep water masses. The principal double-cell structure of the Weddell Gyre is not affected by the ice shelf-ocean interaction, but the western cell is shifted farther offshore by the presence of the lighter water masses from the cavities. These mechanisms will be discussed further in a separate paper.

5. Discussion and Conclusions

An Antarctic circumpolar model is used for simulation and sensitivity studies of the Weddell Sea circulation and water mass distribution. The model is driven by climatological (monthly mean) atmospheric and sea ice forcing and includes the sub–ice shelf forcing.

A central result is the pronounced and persistent double-cell structure of the Weddell Gyre and the corresponding maximum transport of 60 Sv, which differs significantly from previous numerical simulations of this area.

For the first time a large-scale general circulation model includes sub–ice shelf cavities. It was shown that the water masses from the sub–ice cavities contribute significantly to the water mass formation along the continental slope. The water mass characteristics throughout the Weddell Sea are affected by the increased stability of the near-surface stratification, preventing deep ocean convection.

The vertical and lateral spreading of newly formed bottom water shows the relative importance of the Berkner and General Belgrano Banks for the Weddell Sea's bottom water renewal, which agrees with *Gordon*'s [1998] findings based on hydrographic measurements.

We attribute the overall good agreement with observations to the combined effects of (1) the southward extension of the model domain into the inner Weddell Sea and toward the grounding line of the major ice shelf areas, (2) the improved surface forcing from a stand-alone sea ice model that is run with high temporal resolution ECMWF atmospheric data, (3) the inclusion of the sub–ice shelf thermohaline forcing, (4) the reduced vertical mixing in case of static instability, and (5) the stretched vertical coordinate of the ocean model, which results in high resolution both near the surface and the bottom. In particular, models that specify a closed boundary at 70°S produce a much weaker coastal current and Weddell Gyre because they exclude a significant part of the wind forcing. Future developments are directed toward higher resolution and full coupling to a dynamic-thermodynamic sea ice model.

References

Bagriantsev, N.V., A.L. Gordon, and B.A. Huber, Weddell Gyre: Temperature maximum stratum, *J. Geophys. Res.*, 94, 8331-8334, 1989.

Baines, P.G., and S. Condie, Observations and modelling of Antarctic downslope flows: A review, in *Ocean, Ice and Atmosphere: Interactions at the Antarctic Continental Margin. Antarct. Res. Ser.*, Vol. 75, edited by S.S. Jacobs and R.F. Weiss, pp. 29-49, AGU, Washington, D.C., 1998.

Barnier, B., P. Marchesiello, A.P. de Miranda, J.-M. Molines, and M. Coulibaly, A sigma-coordinate primitive equation model for studying the circulation in the South Atlantic. Part I: Model configuration with error estimates, *Deep Sea Res. Part I*, 45, 543-572, 1998.

Beckmann, A., and D.B. Haidvogel, Numerical simulation of flow around a tall isolated seamount: Part I: Problem

formulation and model accuracy, *J. Phys. Oceanogr.*, 23, 1736-1753, 1993.

Beckmann, A., and D.B. Haidvogel, A numerical simulation of flow at Fieberling Guyot, *J. Geophys. Res.*, 102, 5595-5613, 1997.

Carmack, E.C., and T.D. Foster, Circulation and distribution of oceanographic properties near the Filchner Ice Shelf, *Deep Sea Res. Part I*, 22, 77-90, 1975.

Fahrbach, E., G. Rohardt, M. Schröder, and V. Strass, Transport and structure of the Weddell Gyre, *Ann. Geophysicae*, 12, 840-855, 1994.

Fahrbach, E., G. Rohardt, N. Scheele, M. Schröder, V. Strass, and A. Wisotzki, Formation and discharge of deep and bottom water in the northwestern Weddell Sea, *J. Mar. Res.*, 53, 515-538, 1995.

Foldvik, A. and T. Kvinge, Conditional instability of sea water at the freezing point, *Deep Sea Res. Part I*, 21, 169-174, 1974.

Foldvik, A., T. Kvinge, and T. Tørresen, Bottom currents near the continental shelf break in the Weddell Sea, in *Oceanology of the Antarctic Continental Shelf, Antarct. Res. Ser.*, Vol. 43, edited by S.S. Jacobs, pp. 21-34, AGU, Washington, D.C., 1985a.

Foldvik, A., T. Gammelsrød, and T. Tørresen, Circulation and water masses on the southern Weddell Sea shelf, of the Antarctic Continental Shelf, *Antarct. Res. Ser.*, Vol. 43, edited by S.S. Jacobs, pp. 5-20, AGU, Washington, D.C., 1985a.

Gade, H.G., Melting of ice in sea water: a primitive model with application to the Antarctic ice shelf and icebergs, *J. Phys. Oceanogr.*, 9, 189-198, 1979.

Gordon, A.L., Western Weddell Sea thermohaline stratification, in *Ocean, Ice and Atmosphere: Interactions at the Antarctic Continental Margin. Antarct. Res. Ser.*, Vol. 75, edited by S.S. Jacobs and R.F. Weiss, pp. 215-240, AGU, Washington, D.C., 1998.

Gordon, A.L., B.A. Huber, H.H. Hellmer, and A. Ffield, Deep and bottom water of the Weddell Sea's western rim, *Science*, 262, 95-97, 1993.

Grosfeld, K., R. Gerdes, and J. Determann, Thermohaline circulation and interaction between ice shelf cavities and the adjacent open ocean, *J. Geophys. Res.*, 102, 15,595-15,610, 1997.

Haidvogel, D.B., J.L. Wilkin, and R.E. Young, A semi-spectral primitive equation ocean circulation model using vertical sigma and orthogonal curvilinear horizontal coordinates, *J. Comput. Phys.*, 94, 151-185, 1991.

Häkkinen, S., Seasonal simulation of the Southern Ocean coupled ice-ocean system, *J. Geophys. Res.*, 100, 22,733-22,748, 1995.

Hellmer, H.H., and D. Olbers, A two-dimensional model for the thermohaline circulation under an ice shelf, *Antarct. Sci.*, 1, 325-336, 1989.

Hellmer, H.H., S.S. Jacobs, and A. Jenkins, Oceanic erosion of a floating Antarctic glacier in the Amundsen Sea, in *Ocean, Ice and Atmosphere: Interactions at the Antarctic Continental Margin. Antarct. Res. Ser.*, Vol. 75, edited by S.S. Jacobs and R.F. Weiss, pp. 83-99, AGU, Washington, D.C., 1998.

Hibler, W.D., III, A dynamic-thermodynamic sea ice model, *J. Phys. Oceanogr.*, 9, 815-846, 1979.

Jackett, D.R., and T.J. McDougall, Stabilization of hydrographic data, *J. Atmos. Oceanic Technol.*, 12, 381-389, 1995.

Johnson, M. R., and A. M. Smith, Seabed topography under the southern and western Ronne Ice Shelf, derived from seismic surveys, *Antarct. Sci.*, 9, 201-208, 1997.

Kottmeier, C., and L. Sellmann, Atmospheric and oceanic forcing of Weddell Sea ice motion, *J. Geophys. Res.*, 101, 20,809-20,824, 1996.

Lemke, P., W.B. Owens, and W.D. Hibler III, A coupled sea ice-mixed layer-pycnocline model for the Weddell Sea, *J. Geophys. Res.*, 95, 9513-9525, 1990.

Mensch, M., R. Bayer, J.L. Bullister, P. Schlosser, and R.F. Weiss, The distribution of tritium and CFCs in the Weddell Sea during the mid-1980s, *Prog. Oceanogr.*, 38, 377-415, 1996.

Mosby, H., The water of the Atlantic Ocean. Scientific Results of the Norwegian Antarctic Expedition 1927-1928, Vol. 11, 131 pp., Oslo, Norway, 1934.

Muench, R.D., and A.L. Gordon, Circulation and transport of water along the western Weddell Sea margin, *J. Geophys. Res.*, 100, 18,503-18,515, 1995.

Nicholls, K.W., Temperature variability beneath Ronne Ice Shelf, Antarctica, from thermistor cables, *J. Geophys. Res.*, 101, 1199-1210, 1996.

Nicholls, K.W., and K. Makinson, Ocean circulation beneath the western Ronne Ice Shelf, as derived from in situ measurements of water currents and properties, in *Ocean, Ice and Atmosphere: Interactions at the Antarctic Continental Margin. Antarct. Res. Ser.*, Vol. 75, edited by S.S. Jacobs and R.F. Weiss, pp. 303-318, AGU, Washington, D.C., 1998.

Nøst, O.A., and A. Foldvik, A model of ice shelf-ocean interaction with application to the Filchner-Ronne and Ross Ice shelves, *J. Geophys. Res.*, 99, 14243-14254, 1994.

Olbers, D.J., V. Gouretski, G. Seiß, and J. Schröter, *Hydrographic Atlas of the Southern Ocean*, 82 pp., Alfred-Wegener-Inst., Bremerhaven, Germany, 1992.

Pacanowski, R.C., and S.G.H. Philander, A model of the seasonal cycle in the tropical Atlantic Ocean, *J. Geophys. Res.*, 91, 14,192-14,206, 1986.

Parkinson C.L., and W.M. Washington, A large-scale numerical model of sea ice, *J. Geophys. Res.*, 84, 311-337, 1979.

Schenke, H.W., H. Hinze, S. Dijkstra, B. Hoppmann, F. Niederjasper, and T. Schöne, The new bathymetric charts of the Weddell Sea: AWI BCWS, in *Ocean, Ice and Atmosphere: Interactions at the Antarctic Continental Margin. Antarct. Res. Ser.*, Vol. 75, edited by S.S. Jacobs and R.F. Weiss, pp. 373-382, AGU, Washington, D.C., 1998.

Schröder, M., and E. Fahrbach, On the structure and the transport of the eastern Weddell Gyre, *Deep Sea Res. Part I*, 46, 501-527, 1999.

Smith, W.H.F., and D.T. Sandwell, Global sea floor topography from satellite altimetry and ship depth

soundings, *Science*, 277, 1956-1962, 1997.

Song, Y., and D.B. Haidvogel, A semi-implicit ocean circulation model using a generalized topography-following coordinate, *J. Comput. Phys.*, 115, 228-244, 1994.

UNESCO, Tenth report of the joint panel on oceanographic tables and standards, *UNESCO Tech. Pap. Mar. Sci.*, 36, 1981.

Webb, D.J., P.D. Killworth, A.C. Coward, and S.R. Thompson, *The FRAM Atlas of the Southern Ocean*, 67 pp., Nat. Environ. Res. Counc., Swindon, England, 1991.

Weppernig, R., P. Schlosser, S. Khatiwala, and R.G. Fairbanks, Isotope data from Ice Station Weddell: Implications for deep water formation in the Weddell Sea, *J. Geophys. Res.*, 101, 25,723-25,739, 1996.

Zhang, Y, and A.J. Semtner, Ocean-ice interaction within the Weddell and Cosmonaut Seas from high resolution models, *Ann. Geophys.*, 16 suppl. II, 592, 1998.

A. Beckmann, H.H. Hellmer, and R. Timmermann, Alfred-Wegener-Institute for Polar and Marine Research, Postfach 120161, D-27515 Bremerhaven, Germany.
(e-mail: beckmann@awi-bremerhaven.de;
hhellmer@awi-bremerhaven.de;
rtimmerm@awi-bremerhaven.de)